Chapter 9
Probability Bounds Analysis Applied to Multi-purpose Crew Vehicle Nonlinearity

Daniel C. Kammer, Paul Blelloch, and Joel Sills

Abstract The Multi-purpose Crew Vehicle (MPCV) Program Orion finite element model (FEM) was updated based on a modal test performed by Lockheed Martin. Due to nonlinearity observed in the test results, linear low force level (LL) and high force level (HL) FEMs were developed for use during various Space Launch System (SLS) flight regimes depending on expected forcing levels. Uncertainty models were derived for the combined MPCV and MPCV Stage Adaptor LL and HL Hurty/Craig-Bampton (HCB) components based on the MPCV structural test article Configuration 4 modal test-analysis correlation results. Subsequently, system-level uncertainty quantification analyses were performed using both models for various SLS flight configurations to determine the impact of the nonlinearity on important system metrics. The system metrics included both transfer functions associated with attitude control and dynamic loads associated with aerodynamic buffeting during ascent. In each case, an independent Monte Carlo (MC) analysis was performed, and no attempt was made to combine the results. The hybrid parametric variation (HPV) method was used to develop the LL and HL MPCV HCB uncertainty models. The HPV method provides both parametric and non-parametric components of uncertainty. The non-parametric uncertainty accounts for the difference in model form between the linearized analytical model and the corresponding linearized component test results in the form of mode shapes and frequencies at that force level. This linear model-form uncertainty is implemented in the HPV method using random matrix theory. However, the HPV uncertainty models developed for the linear LL and HL MPCV components do not account for the nonlinearity in the MPCV. With respect to the linearized models, this nonlinearity is also an uncertainty in model form, but in this case, it must be treated independently as an epistemic uncertainty. It represents a lack of knowledge, in contrast to an aleatory uncertainty due to the randomness of a variable. In the case of an epistemic variable, the true value is unknown, only the interval within which it lies is known. Epistemic uncertainty can be reduced with increased knowledge, while in general, aleatory uncertainty cannot. This work combines the epistemic uncertainty due to the MPCV nonlinearity with the parametric and non-parametric uncertainty within the HPV method using a second-order propagation approach. The LL and HL test data is augmented with surrogate test data derived from a nonlinear MPCV representation. The impact of the MPCV nonlinearity on system response statistics is determined using a series of cumulative distribution functions in the form of a horsetail plot, or p-box. This results in an interval of probabilities for a specific response value or an interval of response values at a specific probability.

Keywords Uncertainty quantification · Hurty/Craig-Bampton · Random matrix · Model form

Acronyms

C4	Configuration 4
CCDF	Complementary cumulative distribution function
CDF	Cumulative distribution function
CLA	Coupled loads analysis
CMA	Crew module adapter

D. C. Kammer (✉) · P. Blelloch
ATA Engineering, Inc, San Diego, CA, USA
e-mail: daniel.kammer@wisc.edu; paul.blelloch@ata-e.com

J. Sills
NASA Johnson Space Center, Houston, TX, USA
e-mail: joel.w.sills@nasa.gov

Z. Mao (eds.), *Model Validation and Uncertainty Quantification, Volume 3*, Conference Proceedings of the Society for Experimental Mechanics Series, https://doi.org/10.1007/978-3-031-04090-0_9

CS	Core stage
dB	Decibel
DCGM	Diagonal cross-generalized mass
DOF	Degree of freedom
FI	Fixed-interface
FEM	Finite element model
HCB	Hurty/Craig-Bampton
HL	High load
HPV	Hybrid parametric variation
Hz	Hertz
itRGA	Intertank rate gyro assembly
lbf	Pound force
lbf-in	Pound-force inch
LAS	Launch abort system
LL	Low load
MC	Monte Carlo
MPCV	Multi-purpose Crew Vehicle
MSA	MPCV Stage Adapter
PDF	Probability distribution function
QOI	Quantity of interest
RMS	Root mean square
SLS	Space Launch System
SOP	Second-order propagation
UQ	Uncertainty quantification

9.1 Introduction

The Multi-Purpose Crew Vehicle (MPCV) Program Orion finite element model (FEM) was updated based on a modal test performed at the Lockheed Martin facility in Denver, from October 2017 to July 2018. Due to nonlinearity observed in the test results, linear low force level (LL) and high force level (HL) FEMs were developed for use during various Space Launch System (SLS) flight regimes depending on expected forcing levels. Uncertainty models were developed for the combined MPCV and MPCV Stage Adaptor (MSA) LL and HL Hurty/Craig-Bampton (HCB) [1] components based on the MPCV structural test article (STA) Configuration 4 (C4) modal test-analysis correlation results. Subsequently, system-level uncertainty quantification (UQ) analyses were performed using both models for various SLS flight configurations to determine the impact of the nonlinearity on important system metrics. The system metrics included both transfer functions associated with attitude control at 120 s after liftoff and dynamic loads associated with aerodynamic buffeting at 50 s after liftoff. In each case, an independent Monte Carlo (MC) analysis was performed, and no attempt was made to combine the results.

The hybrid parametric variation (HPV) method [2–4] was used to develop the LL and HL MPCV/MSA HCB uncertainty models. The HPV method provides both parametric and non-parametric components of uncertainty. The non-parametric uncertainty accounts for the difference in model form between the linearized analytical model and the corresponding linearized component test results in the form of mode shapes and frequencies at that force level. This linear model-form uncertainty is implemented within the HPV method using random matrix theory. The parametric part of HPV treats the modal frequencies as uncertain parameters and layers that on top of the random matrices. However, the HPV uncertainty models developed for the linear LL and HL MPCV/MSA components do not directly account for the nonlinearity observed in the MPCV. With respect to the linearized models, this nonlinearity can be considered an uncertainty in model form, but in this case, it must be treated independently as an epistemic uncertainty since the structure will be exercised at a range of input levels during flight. It represents a lack of knowledge, in contrast to an aleatory uncertainty due to the randomness of a variable. In the case of an epistemic variable, the true value is unknown, only the interval within which it lies is known. Epistemic uncertainty can be reduced with increased knowledge, while in general, aleatory uncertainty cannot. In an MC analysis, an aleatory variable is sampled according to a designated probability distribution, while an epistemic variable cannot, not even when using a uniform distribution [5, 6]. Doing so can produce incorrect and misleading results [5].

This work combines the epistemic uncertainty due to the MPCV nonlinearity with the parametric and non-parametric uncertainty within the HPV method using a second-order propagation approach (SOP). Initially, only the LL and HL test data are considered in the analysis. However, the LL and HL test data are then augmented with surrogate test data derived from a simulation using a nonlinear MPCV representation. The impact of the MPCV nonlinearity on system response statistics is determined through the use of a series of cumulative distribution functions (CDF) in the form of a horsetail plot, or p-box. This results in an interval of probabilities for a specific response value or an interval of response values at a specific probability.

9.2 Combining Epistemic and Aleatory Uncertainty

Epistemic and aleatory variables can be combined within a single UQ analysis using an SOP approach [6, 7]. Within this technique, there are two loops, as shown in Fig. 9.1. In the outer loop, the epistemic variables are sampled from within their respective intervals. Their values are then passed as deterministic variables to the inner loop, where the aleatory variables are sampled from their respective probability distributions. For each set of epistemic variable values, an MC analysis is performed on the aleatory variables, resulting in a corresponding CDF for each selected quantity of interest (QOI). The complete UQ analysis produces an ensemble of CDFs, sometimes called a horsetail plot [6]. The interpretation is that each CDF within the ensemble has no relative probability of occurrence, only that each is possible [7]. Bounds on the ensemble of CDFs are called a probability box (p-box) [8]. Figure 9.2 illustrates a general p-box with bounds $L(x)$ and $U(x)$ for uncertain QOI x.

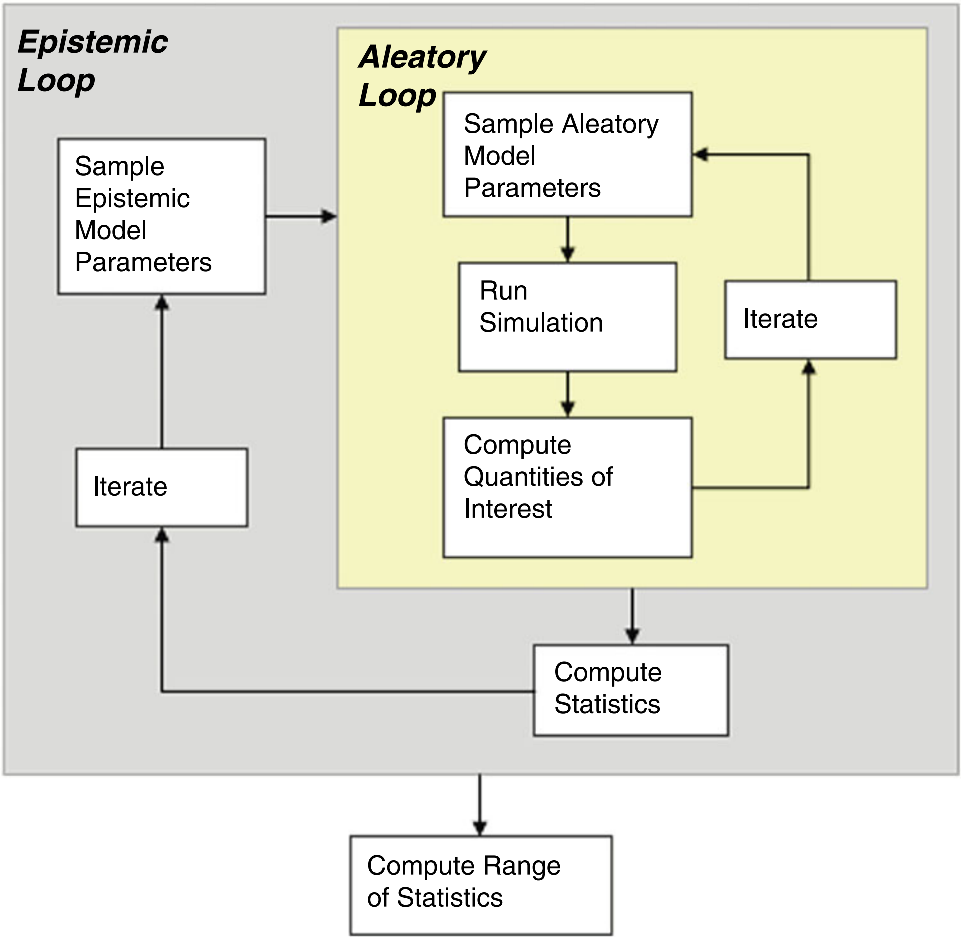

Fig. 9.1 Flow diagram for SOP [8]

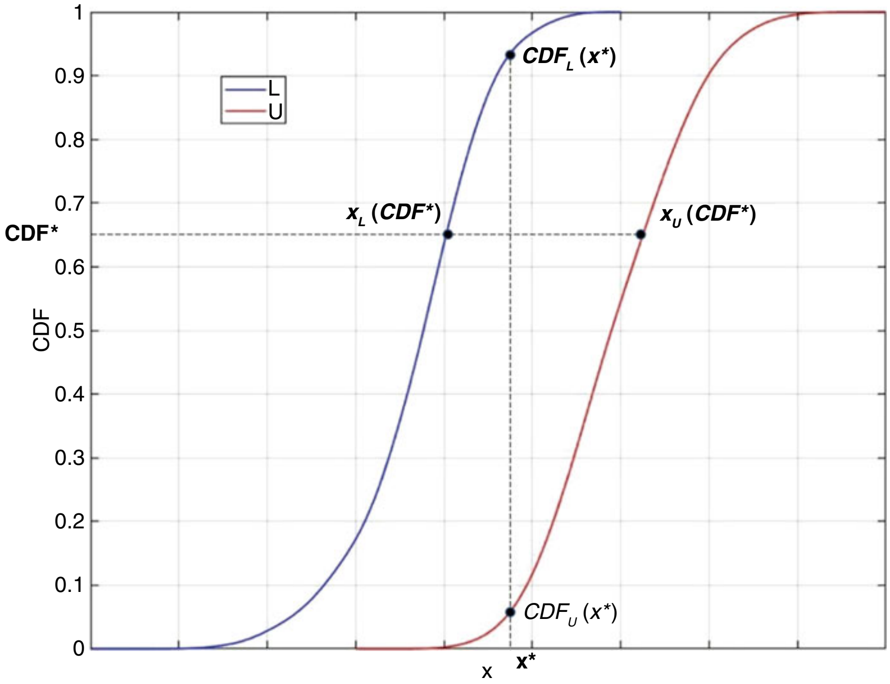

Fig. 9.2 General p-box for uncertain variable *x*

For a horizontal line drawn at a selected value CDF*, the p-box provides an interval of plausible variable *x* values. This means that the response at a specific probability level lies within a range of response values, not just at a single value [6]. The CDF value is deterministic, and all the uncertainty is in the variable *x* [9]. Conversely, for a vertical line at the selected variable value *x**, the p-box gives an interval of plausible probabilities. In this case, the variable is deterministic, and the uncertainty lies in the CDF. Combining epistemic and aleatory uncertainty in this fashion determines the range of the QOI that corresponds to a certain percentile and the range of percentiles that corresponds to a specific value of the QOI [8].

9.3 SOP UQ Applied to SLS

In the case of the SLS, the individual HPV UQ assessments are performed using MPCV models that can be thought of as linearizations of the nonlinear model representing the true MPCV. There are no specific epistemic variables that govern the observed nonlinearity or model from uncertainty that can be sampled in the SOP outer loop. Instead, the MPCV nonlinearity can be thought of as being simplistically represented by a slider that gives the mapping from the nonlinear model into the linearized model at a specific forcing level. Discretely adjusting the slider over the forcing level interval of interest would produce an outer loop represented by an ensemble of linear models that approximate the nonlinear model at a corresponding ensemble of input force levels. For each linearized model, the SOP inner loop corresponds to the application the HPV UQ method using an MC analysis. In the case of the MPCV nonlinearity, there are only two members in the ensemble of linearized system models: one containing the LL MPCV and one containing the HL MPCV. Therefore, the SOP consists of two MC analyses, one using the LL system model and one using the HL model. Ideally, these two models would provide CDFs that would bound the effects of the MPCV nonlinearity for the QOIs, but there is no guarantee that is the case.

This method is approximate in the sense that no linear model exactly captures the nonlinear behavior, even at a fixed input level. This is due to the fact that even the behavior of a single degree of freedom system with a nonlinear spring can only be approximated by a linear spring and also because a complex system has many modes, each of which will result in different behavior at nonlinear joints. This is addressed in the current approach by finding the linear model that best captures the nonlinear behavior at each force level and then adding uncertainty to that best fit linear model to represent the fact that it only approximates the nonlinear behavior at that force level.

To perform the system level UQ, the SLS system is broken into five primary “components.” These are the two solid rocket booster (SRBs), the core stage, the 2nd stage, and the MPCV/MSA. Uncertainty models based on modal test results are

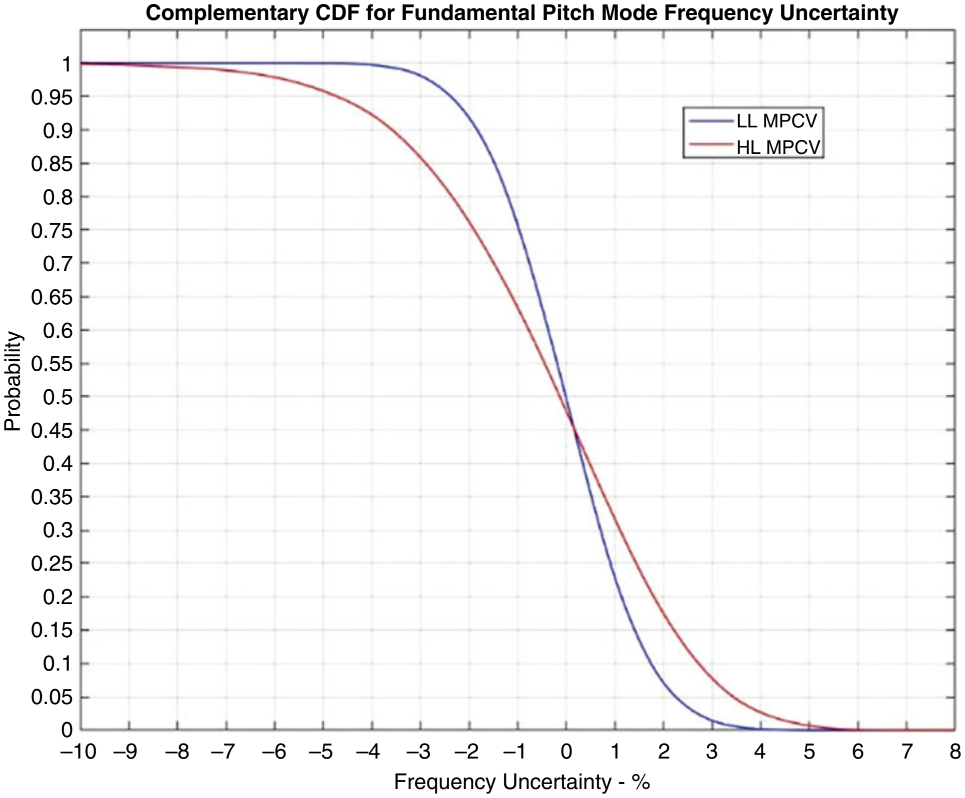

Fig. 9.3 Complementary CDFs for LL and HL MPCV pitch frequency uncertainty

applied to all five components. Details related to these components and their uncertainty models can be found in references [2, 3]. In this work, only the MPCV/MSA component is treated as an epistemic uncertainty to cover nonlinear response.

9.3.1 Guidance Navigation and Control

The first application of the SOP approach is to the guidance, navigation, and control attitude stability conditions for the SLS configuration corresponding to ascent at liftoff T0 + 120 s, prior to booster separation. The uncertainty in the fundamental bending mode frequencies must be greater than −10%, and the corresponding frequency response gain uncertainty must be less than 4 dB to guarantee control system stability. Figure 9.3 shows the complementary CDFs (CCDFs) (i.e., cumulative probability of being greater than) for the uncertainty in the LL and HL fundamental pitch frequencies based on an inner-loop MC analysis with 10,015 iterations. Figure 9.4 presents an expanded view of Fig. 9.3. If a vertical line is drawn at the lower bound for frequency uncertainty (i.e., −10%), then the plausible range in probability is between P99.8 and P100. At a frequency uncertainty of −5%, a vertical line indicates a plausible range in probability of between P95.8 and P100. Conversely, drawing horizontal lines at probability values of P90, P95, and P99 produces plausible ranges of pitch frequency uncertainty, as listed in Table 9.1. These plausible ranges of probability and QOI are due to the model-form uncertainty represented by the linearized LL and HL MPCV models. At the lower bound of allowed frequency uncertainty, the MPCV nonlinearity produces almost no uncertainty.

Figure 9.5 presents the CCDFs for the uncertainty in the LL and HL fundamental yaw bending frequencies. The order of the CCDFs is the opposite of what it was in the case of pitch because the PDF for the LL yaw frequency has a greater standard deviation than that for the HL PDF. The spread in frequency uncertainty between the LL and HL models for yaw is not as great as it is in the case of pitch, shown in Fig. 9.3. If a vertical line is drawn at the lower bound for frequency uncertainty (i.e., −10%), there is no plausible range in probability. If a vertical line is drawn at −5%, the plausible range in probability is between P95.7 and P97.7. Conversely, drawing horizontal lines at probability values of P90, P95, and P99 produces plausible ranges of yaw frequency uncertainty listed in Table 9.2. The plausible ranges of probability and frequency uncertainty for

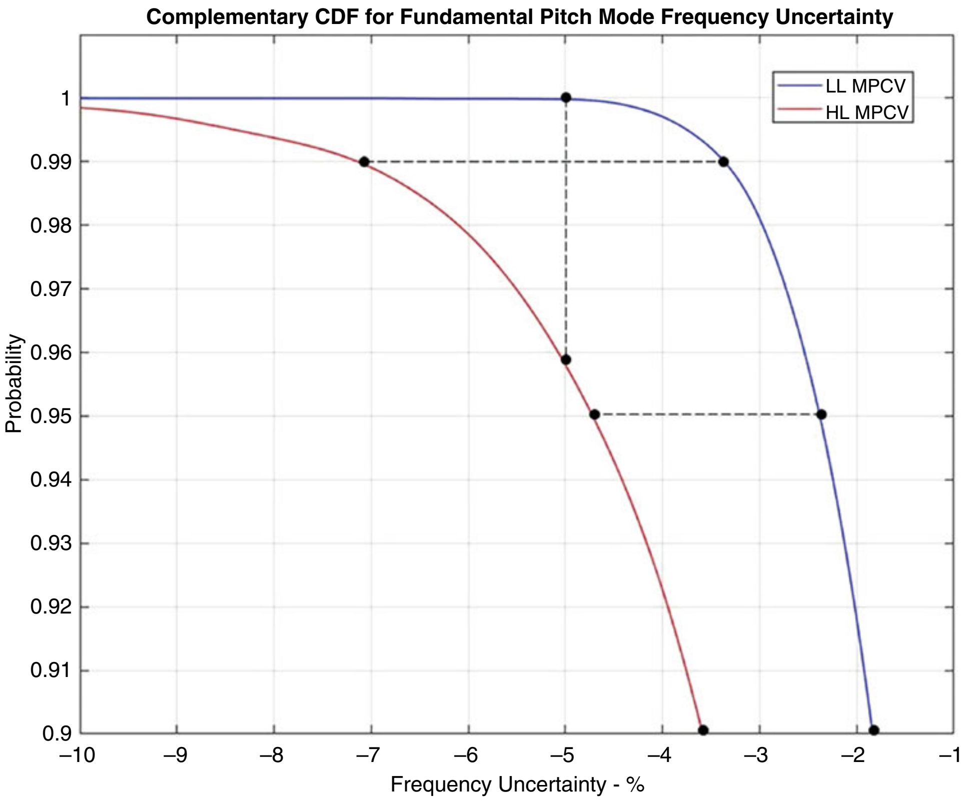

Fig. 9.4 Expanded view of CCDFs for LL and HL MPCV pitch frequency uncertainty

Table 9.1 Plausible range of pitch frequency uncertainty

	Range of uncertainty – %		Delta – %
Probability	HL	LL	abs([HL-LL]/LL)
90	−3.60	−1.85	94.59
95	−4.70	−2.40	95.83
99	−7.15	−3.35	113.43

yaw are smaller than for pitch, indicating that the MPCV nonlinearity has a greater impact on the system fundamental pitch bending frequency than the fundamental yaw bending frequency.

Uncertainty in pitch and yaw rate gains can be examined in the same way. Figure 9.6 illustrates the CDFs for the uncertainty in the pitch rate gain at the core stage intertank rate gyro assembly (itRGA) for the ascent at T0 + 120 s configuration. If a vertical line is drawn at the 4 dB upper bound for gain uncertainty, the corresponding plausible range in probability is between P99.9 and P100. Drawing horizontal lines at probability values of P90, P95, and P99 produces plausible ranges of pitch rate gain uncertainty listed in Table 9.3. Figure 9.7 shows the CDFs for the corresponding uncertainty in the yaw rate gain at the itRGA. In this case, the CDFs do not intersect. Drawing a vertical line at the upper bound of 4 dB uncertainty in gain produces a probability of approximately P98.8. There is essentially no range of plausible probabilities for 4 dB uncertainty in pitch or yaw rate gain. This implies that the MPCV nonlinearity has little impact on the percentile corresponding to the 4 dB rate gain uncertainty stability requirement. Table 9.4 lists the plausible ranges of yaw rate gain uncertainty for probabilities P90, P95, and P99. The widths of the plausible ranges for yaw rate gain are smaller than those for pitch, indicating that the nonlinearity in the MPCV has a smaller impact on yaw rate gain than pitch.

9.3.2 Buffet

An SOP analysis was also applied to the SLS core stage (CS) section loads due to buffet at ascent T0 + 50 s. In the original work, it was found that there were appreciable differences in nominal CS peak moments about Y and in peak shear along

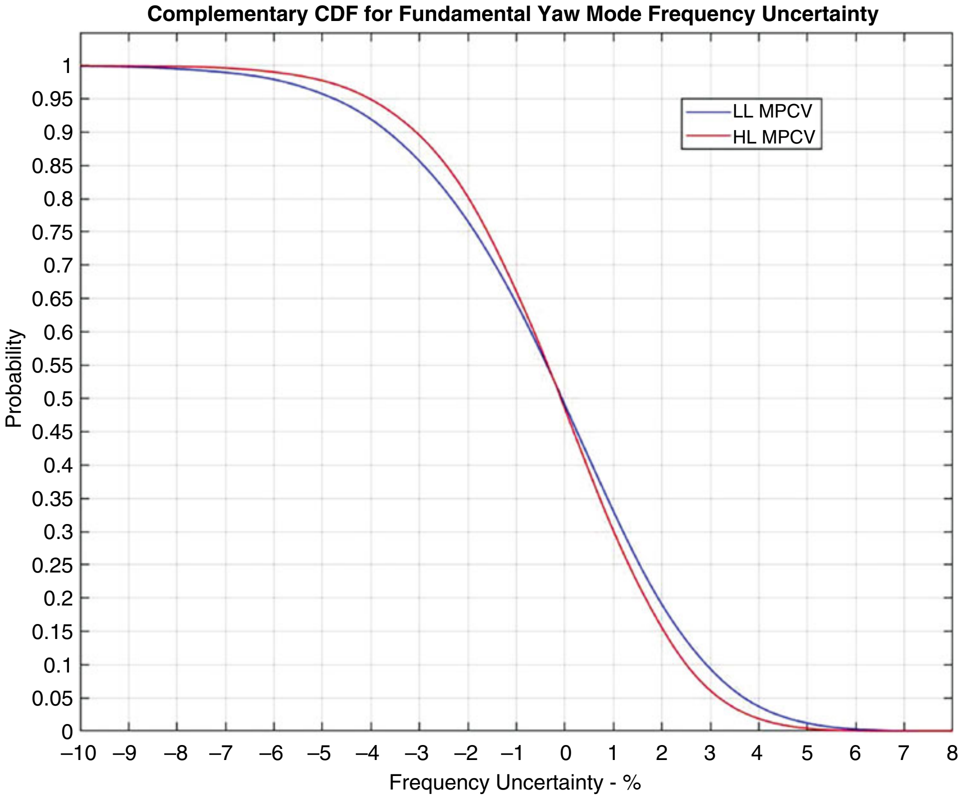

Fig. 9.5 Complementary CDFs for LL and HL MPCV yaw frequency uncertainty

Table 9.2 Plausible range of yaw frequency uncertainty

	Range of uncertainty – %		Delta – %
Probability	LL	HL	abs([HL-LL]/LL)
90	−3.65	−3.05	16.44
95	−4.75	−4.00	15.79
99	−7.05	−6.00	14.89

Z predicted using the LL MPCV model versus the HL MPCV model. The peak moment about Y for the LL MPCV model occurs at section $x = 2754.99$ inches and is approximately 15% higher than that predicted by the HL model. Figure 9.8 illustrates the LL and HL CDFs for the normalized peak moments about Y at $x = 2754.99$ inches for an ensemble of 1000 random systems. No critical value of CS section moment was specified,[1] but as an example, drawing a vertical line at the specific normalized peak moment of 1.4 produces the plausible range of probabilities P34–P95. The MPCV nonlinearity has a large influence on the probability of this specific peak CS moment value. Horizontal lines at probabilities P50 and P90 produce plausible ranges of peak moment about Y listed in Table 9.5.

The peak CS shear along Z occurs at section $x = 2862.71$ inches using the HL MPCV model. It is approximately 11% larger than the value predicted using the LL MPCV. Figure 9.9 presents the LL and HL CDFs for the normalized peak shear along Z. As an example, picking a specific normalized peak shear of 2.4 produces a range of plausible probabilities between P57 and P97. Picking probabilities P50 and P90 yield ranges of peak shear values listed in Table 9.6. Based on these results, the MPCV nonlinearity has a substantial effect upon the statistics for the peak CS moment about Y and the peak CS shear along Z from buffet loading. Percentage wise, the impact is greater on the peak section shear along Z.

---

[1] Vehicle bending moments during atmospheric flight are typically dominated by static aeroelastic loads and gust, with buffet playing a secondary role. The uncertainty in buffet responses, therefore, does not reflect an equivalent uncertainty in peak bending moments experienced by the vehicle.

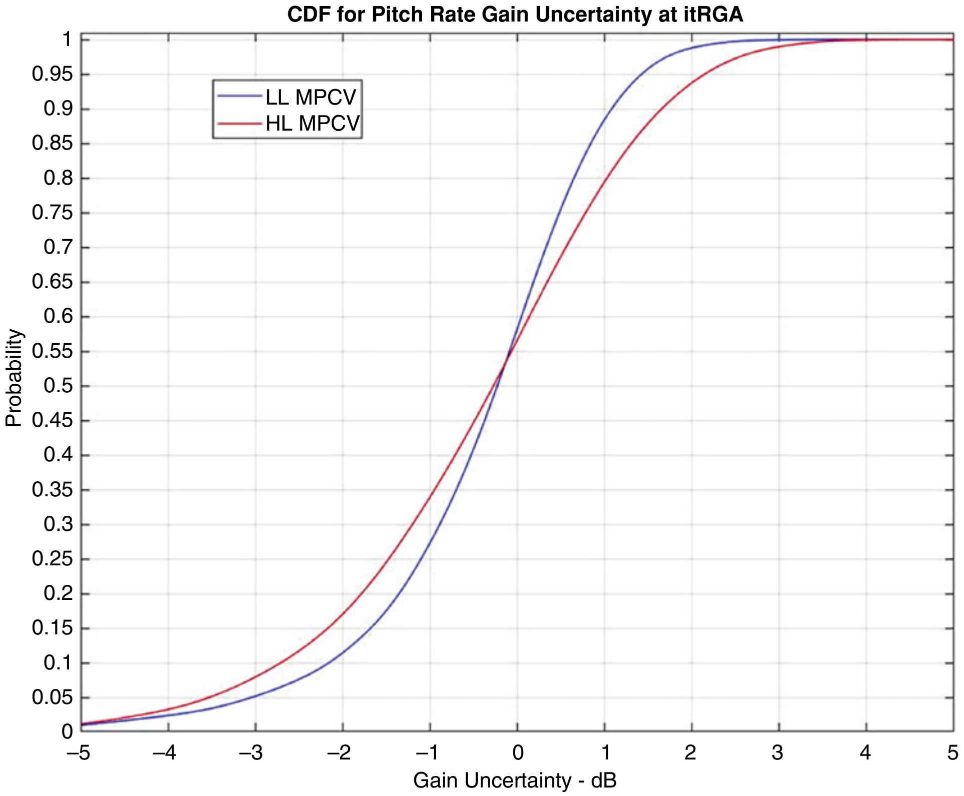

Fig. 9.6 CDFs for LL and HL MPCV pitch rate gain uncertainty

9.4 SOP Analysis of SLS Using Surrogate Test Data

The drawback of the previous analysis is that there are only two sets of C4 test data, one at low input levels and one at high input levels. The two sets of test data were used to generate corresponding LL and HL linear MPCV models. In the LL MPCV model, the nonlinear joints are fixed with respect to relative motion, while in the case of the HL model, they are modeled with relatively low stiffness and are effectively free to slip. The corresponding model ensemble describing the SOP outer loop contains only two models. This results in response horsetail plots that contain only two CDFs, which assumes that the LL and HL responses bound the corresponding p-boxes. While the original program goal was to bound the response of the nonlinear MPCV by using both the LL and HL linear MPCV models, there is no guarantee that this is the case.

Ideally, additional C4 modal test data would have been measured at intermediate loading levels in order to study MPCV nonlinearity. Since this was not done, this work augments the C4 test data with surrogate test data generated using a nonlinear model of the MPCV that captures the friction behavior of the joints. Eight additional linear MPCV models were generated based on simulated response to enforced base sine inputs of amplitudes 0.1, 1, 2, 3, 5, 7.5, 10, and 20 in/s^2. At the input level of 0.1 in/s^2, the nonlinear joints are essentially fixed, as in the LL MPCV. In contrast, at an input level of 20 in/s^2, the joints are freely slipping, as in the HL MPCV. SOP UQ analysis is performed for each of the additional eight models in the ensemble. The goal is to determine how well the LL and HL MPCV models bound the response of the actual nonlinear MPCV based on linearized models.

9.4.1 Generation of Linear MPCV Models Based on Surrogate Test Data

Since actual test data was only available for the LL and HL responses, surrogate test data was developed by running a nonlinear MPCV model. This model was initially based on reducing a NASTRAN FEM to the sliding interfaces along with additional nodes for recovery of responses in an HCB format. This was then transformed to an ABAQUS substructure using the *MATRIX INPUT format. The slipping joints were modeled as 204 *CONNECTOR elements corresponding to

Table 9.3 Plausible range of pitch rate gain uncertainty

	Range of uncertainty – dB		Delta – %
Probability	LL	HL	abs([HL-LL]/LL)
90	1.08	1.64	51.85
95	1.42	2.14	50.70
99	2.07	3.01	45.41

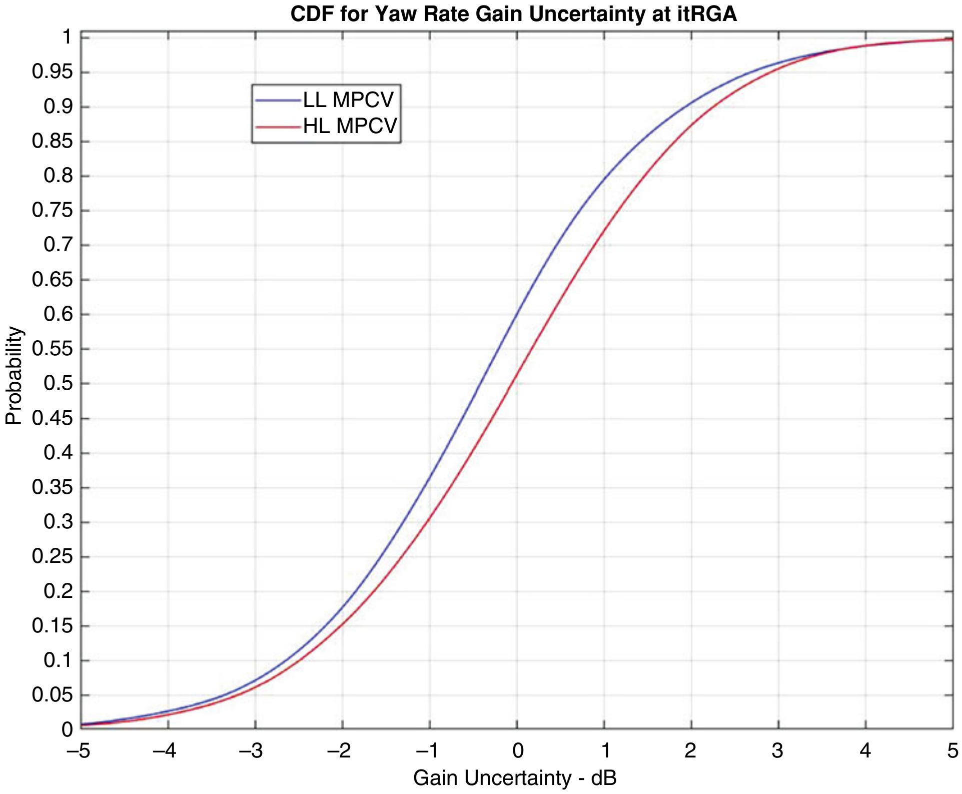

Fig. 9.7 CDFs for LL and HL MPCV yaw rate gain uncertainty

Table 9.4 Plausible range of yaw rate gain uncertainty

	Range of uncertainty – dB		Delta – %
Probability	LL	HL	abs([HL-LL]/LL)
90	1.93	2.25	16.58
95	2.68	2.91	8.58
99	4.10	4.14	0.98

the airfoils between the crew module adaptor (CMA) and fairing and 114 *CONNECTOR elements corresponding to the aerodeflectors between the launch abort system (LAS) and CMA, as illustrated in Fig. 9.10. All other connections were assumed to be linear. Each joint is a two degrees of freedom (DOFs) sliding joint in the 2 and 3 directions. Since all the corresponding elements are defined in a cylindrical coordinate system, this is a joint that's fixed radially and sliding tangentially and vertically.

The ABAQUS connector elements represent a sliding interface like the one illustrated in Fig. 9.11, where K1 is the "sliding stiffness," K2 is the "stick stiffness," and μ is the "friction force," which is the product of the normal force and the coefficient of friction. Different K1, K2, and m values were used for the airfoil and the aerodeflector joints, based on tuning the nonlinear model to modal test results. Note that the ABAQUS connector elements are two-dimensional versions of the system illustrated in Fig. 9.12, since they slide in the tangential/vertical plane. The parameters were originally tuned to approximately fit the nonlinear behavior observed at the LL and HL excitation levels. Initially the goal was to use the ABAQUS model directly and exercise it at different input levels. However, 10 s of simulation took up to 10 days of run time, so it was not feasible to generate the data required for this study using that approach.

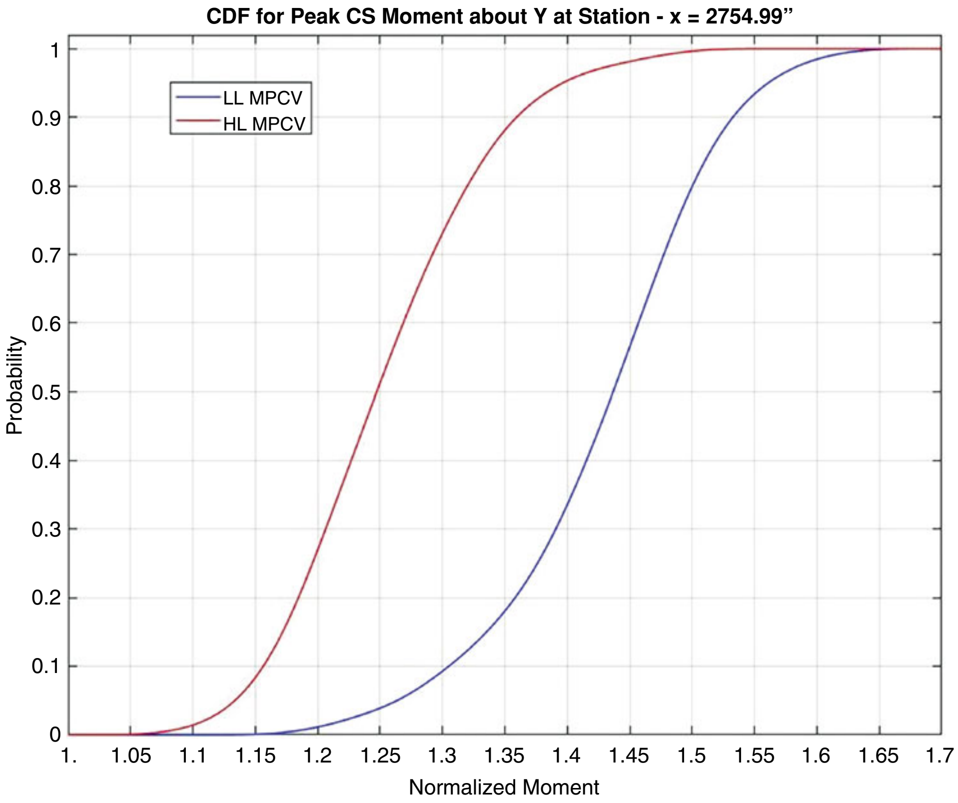

Fig. 9.8 CDFs for LL and HL MPCV peak CS moment about Y at $x = 2754.99$ inches

Table 9.5 Plausible range of peak moment about Y at $x = 2754.99$ inches

Probability	Range – % abs([HL-LL]/LL)
50	11.61
90	9.99

An alternate approach was developed using ATA's internal Matlab nonlinear integration algorithm. This code was developed to support coupled loads analysis (CLA) and other dynamic response calculations where local nonlinearities are critical to the response. It uses a Chapman algorithm [10] to integrate the equations along with a user supplied function to represent the nonlinear forces. This approach is based on modal properties calculated in Nastran, with residual vectors at the nonlinear joints to accurately capture local compliance. A user supplied routine was developed and checked that captured the one-dimensional version of the sliding joint illustrated in Fig. 9.11. In this case the sliding stiffness (K1) was included in the Nastran model, while the friction force (μ) and the stick stiffness (K2) were included in the user supplied routine. Each two-dimensional joint was represented by two one-dimensional elements. This is not identical to the representation in ABAQUS, but it captures the observed behavior as the input is increased. A total $2 \times (204 + 114)$ sliding elements were included in the model.

Behavior of the joints was validated by first exercising the function directly and then exercising it in the context of the MPCV model and examining the force/deflection curves over a range of input levels. Force/deflection curves for all the sliding elements at various input levels are illustrated in Fig. 9.12. At the lowest level input, the joints are acting as stiff linear springs, with a spring constant equal to the stick stiffness of each joint. As the input level is increased, each joint travels in a hysteretic loop, with increasing slip, but with a force that never exceeds the friction force in the joint. While the exact behavior of the pairs of one-dimensional joints is a little different from the two-dimensional joint modeled in ABAQUS, the expected behavior from fully stuck to fully sliding and the corresponding shift in frequency was captured using this approach. Run times were reduced to approximately 2 h for 50 s of simulation or a 600X improvement over the ABAQUS run times.

Initially, scaled versions of the random buffet forcing functions were applied at the base of the MPCV to exercise the nonlinear joints at different levels of excitation. However, the random buffet input resulted in very poor frequency response

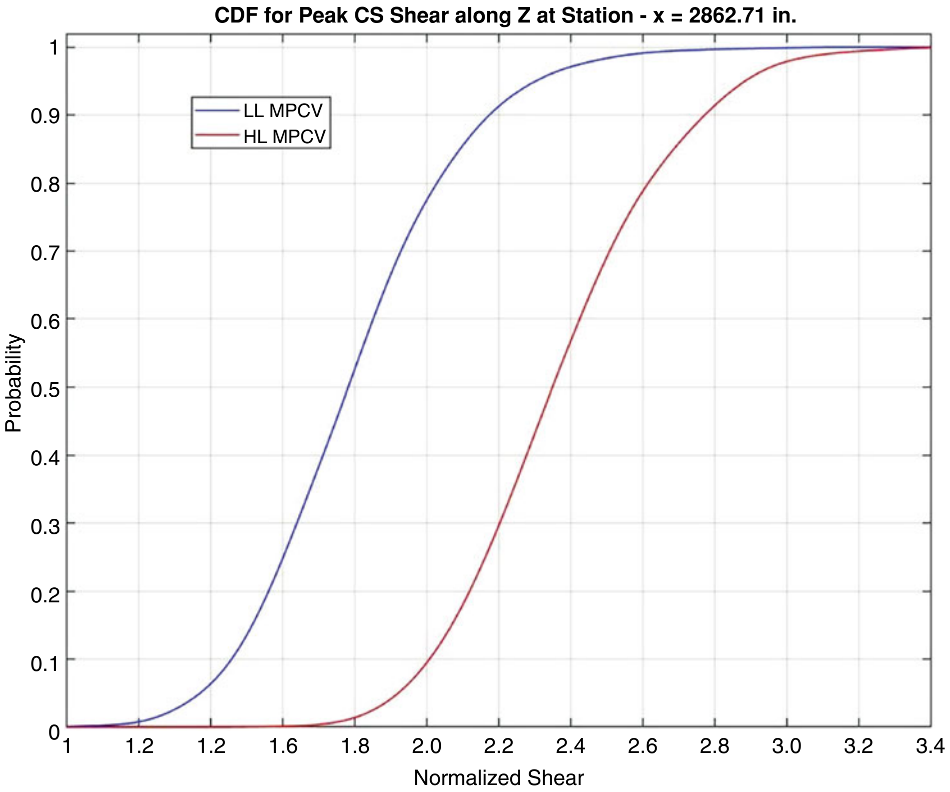

Fig. 9.9 CDFs for LL and HL MPCV peak CS shear along Z at $x = 2862.71$ inches

Table 9.6 Plausible range of peak shear along Z at $x = 2862.71$ inches

	Range – %
Probability	abs([HL-LL]/LL)
50	13.46
90	13.03

function estimates, so a wrapped frequency multi-sine swept input applied as an enforced acceleration in all three directions at the base was used instead. The sweeps are logarithmic from 20 Hz to 1 Hz. The first axis (X) starts at 20 and sweeps down to 1 Hz; the second axis (Y) starts at 8 Hz, sweeps down to 1 Hz, starts back up at 20 Hz, and sweeps down to 8 Hz; the third axis (Z) starts at 3 Hz sweeps down to 1 Hz, starts back up at 20 Hz, and sweeps down to 3 Hz. The signal frequencies vs. time are illustrated in Fig. 9.13. This approach results in three independent signals that can be separated from each to calculate transfer functions from each of the three inputs to 1029 response accelerations on the MPCV.

Each simulation used a constant amplitude sine input as a function of frequency, so the only variation was in the amplitude of the signal. Several different amplitudes were applied to examine the behavior of the joints and find a range of amplitudes that would exercise the joints through their full range. An input amplitude of 0.1 in/s^2 was found to result in linear behavior as illustrated in Fig. 9.12. As the amplitude was increased, modal properties reached asymptotic limits as the input approached roughly 20 in/s^2. Based on this observation, the MPCV nonlinear model was simulated at input amplitudes of 0.1, 1, 2, 3, 5, 7.5, 10, and 20 in/s^2. Transfer functions from the three inputs to 1029 outputs were calculated for each input level. The transfer function from Y input to Y response on the LAS ballast node is illustrated in Fig. 9.14. Results are similar in the X and Z direction.

Next the OPOLY™ modal fitting algorithm was used to estimate a set of linear modes associated with each set of transfer functions. To maintain consistency across force levels, a total of eight modes were fit to each level. These included the 1st axial mode, the 1st four Y-bending modes,[2] and the 1st three Z-bending modes. The variation in frequency of these eight modes as a function of input level is illustrated in Fig. 9.15. The frequency variations were like those observed in

---

[2] All levels identified a pair of fairly closely spaced bending modes in the Y-direction, which were not observed in the Z-direction, resulting in 4 Y-bending and 3 Z-bending modes in the frequency range.

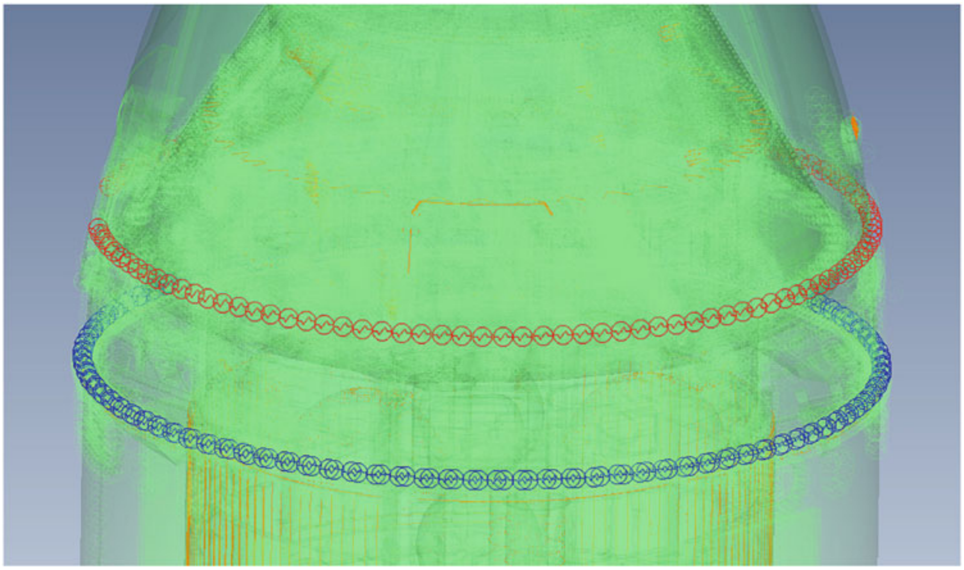

Fig. 9.10 Location of 204 airfoil (blue) and 114 aerodeflector (red) nonlinear joints in MPCV FEM

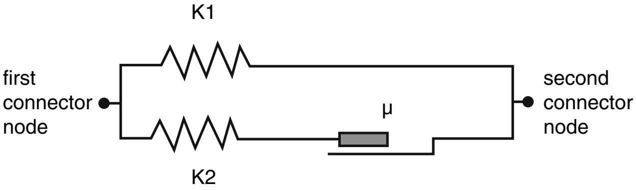

Fig. 9.11 Nonlinear model for airfoil and aerodeflector joints

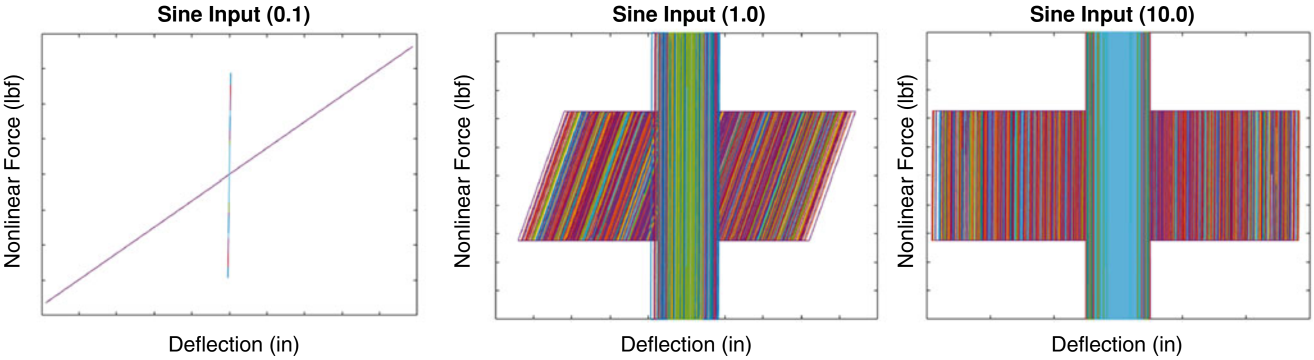

Fig. 9.12 Force/deflection curves for MPCV sliding joints at various input levels

the correlation study for the MPCV LL and HL loads. The axial frequency drops by about 11%. The 1st bending mode frequencies in the Y and Z directions drop by 14% and 25%, respectively. All other bending modes drop in frequency, though by different amounts.

The final step was to "tune" a FEM to match the observed results at each input level. This was done by parameterizing the FEM using the axial and tangential stiffness values at each of the two joint types. ATA's ATTUNE™ software, which uses a genetic algorithm to find a set of FEM properties that best match the measured frequencies, was then applied to find optimal values of the four parameters. Since the individual joints are not necessarily slipping identically, and since the joints slip differently in different modes, it isn't possible to find one set of spring values that will match all frequencies at each input level. The algorithm uses a sum of squares error metric to find an optimal solution, and the lower frequency modes were weighted a little more heavily than the higher frequency modes. The normalized values of the optimally tuned spring stiffnesses for each input level are plotted in Fig. 9.16. In this case 0% is the "slipping" value, while 100% is the "stick" value.

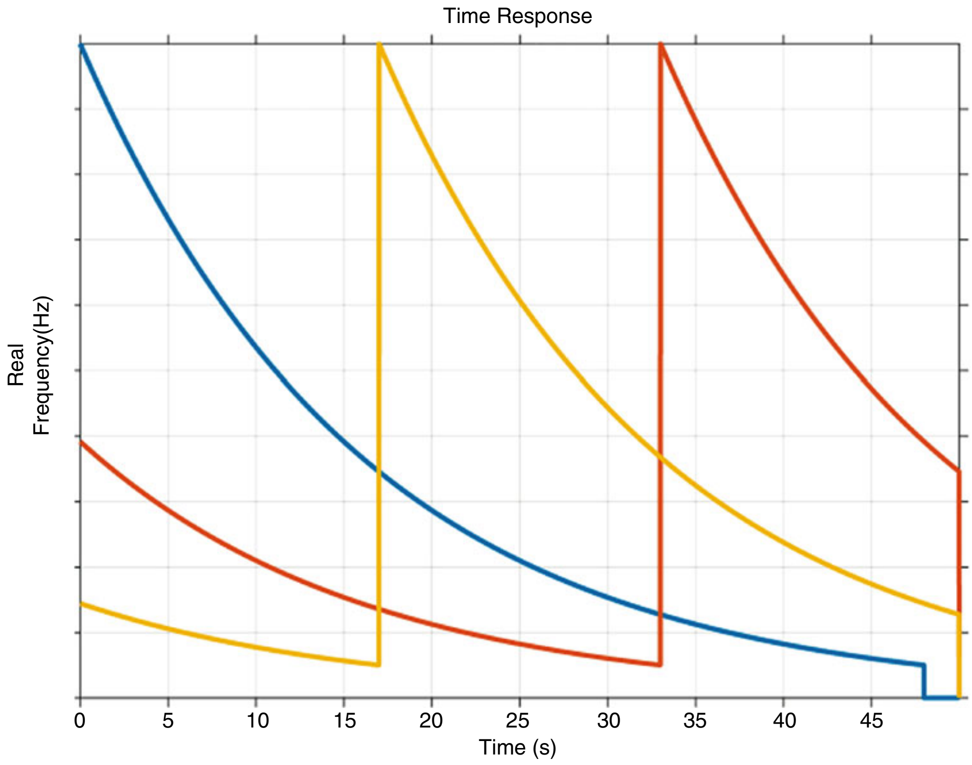

Fig. 9.13 Input base shake frequencies in X, Y, and Z direction as a function of time

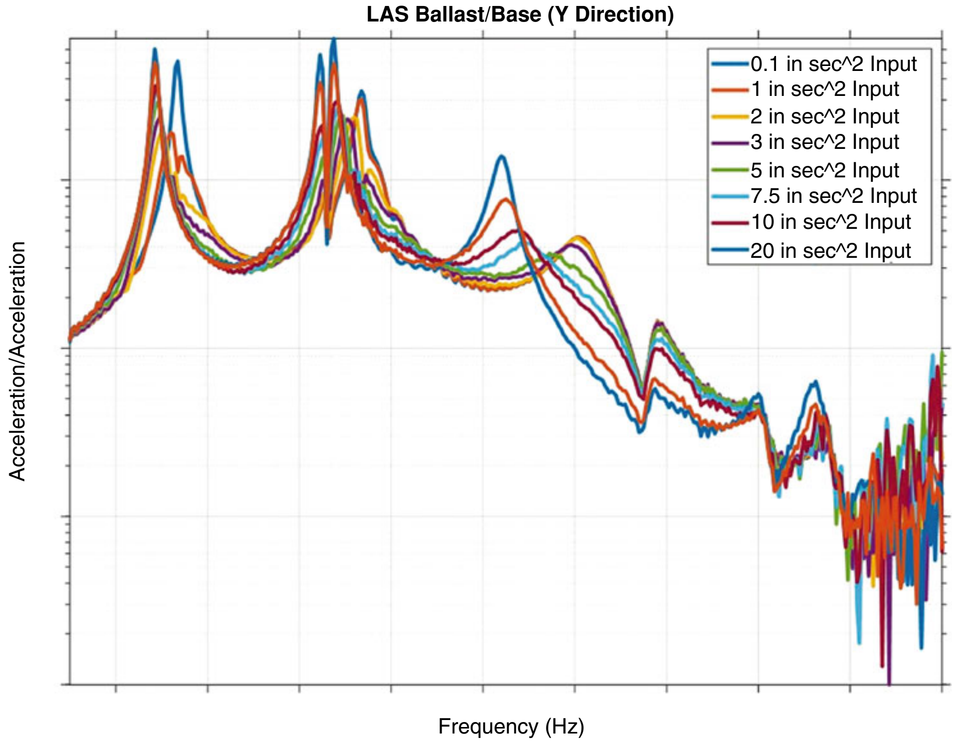

Fig. 9.14 Y Direction transfer functions for different input levels

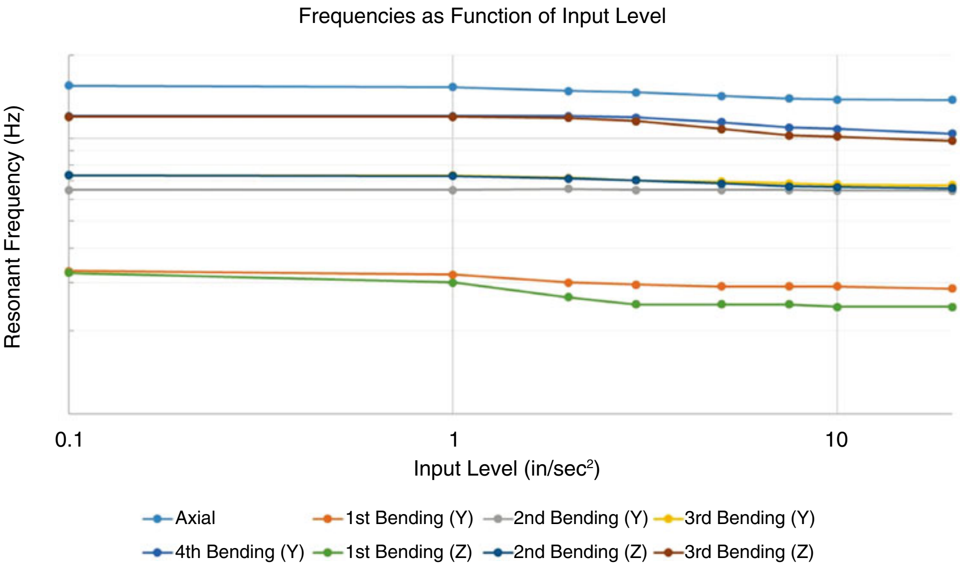

Fig. 9.15 Variation in frequency as a function of base acceleration input level

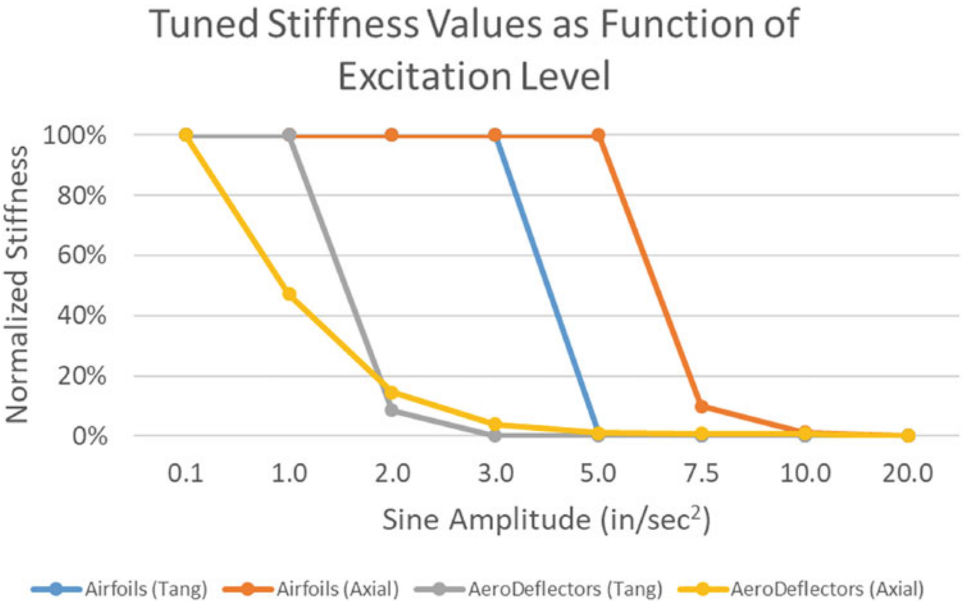

Fig. 9.16 Optimal normalized spring stiffness as a function of base acceleration input level

It is interesting to note that the optimal fits suggest that the joints begin to slip at different input levels. The aerodeflectors slip first in the axial direction and then tangential direction. The airfoils, on the other hand, don’t begin to slip until an input level of 5 in/s^2, first axially and then tangentially. All spring values have reached their asymptotic “slipping” values by an input level of 10 in/s^2. In all cases the slipping behavior is approximate because the joints behave differently in different modes at different frequencies. This means that no one spring stiffness can capture even the linearized behavior of all the modes. This is addressed by finding a compromise solution that matches the target modes as well as possible “on the average” and then accounting for the fact that it does not match all modes in the uncertainty model.

The MPCV FEM was reduced to the 1029 “measured” DOFs in order to provide an orthogonality metric to match modes and calculate a mode shape error. Because no one set of the four spring stiffness parameters can match all modes, the modal error varies from level to level, and this was used to inform the uncertainty models described in the next section.

Table 9.7 Test-analysis frequency error (%) for first nine test modes

	Input level – in/s^2							
Test mode	0.1	1	2	3	5	7.5	10	20
1	0.52%	0.12%	1.31%	1.93%	0.70%	0.74%	0.64%	0.60%
2	0.05%	1.51%	1.73%	0.22%	0.49%	0.03%	0.18%	0.11%
3	0.25%	0.40%	0.23%	1.74%	1.36%	1.35%	1.04%	0.01%
4	0.99%	0.94%	0.43%	2.61%	1.87%	1.42%	0.96%	0.08%
5	1.36%	4.45%	10.30%	12.06%	9.55%	4.92%	3.32%	0.06%
6	1.03%	3.33%	8.06%	10.22%	9.23%	5.42%	3.72%	0.04%
7	0.27%	0.94%	1.25%	1.39%	1.35%	1.30%	1.04%	0.01%
8	0.36%	0.76%	1.20%	2.86%	1.04%	0.27%	0.42%	0.56%
9	0.81%	1.89%	2.24%	1.09%	0.99%	0.93%	0.34%	0.38%
Mean	0.63%	1.59%	2.97%	3.79%	2.95%	1.82%	1.30%	0.20%

9.4.2 Uncertainty Models for MPCV/MSA HCB Components

An HPV component uncertainty model is based on the HCB component representation. Uncertainty in the HCB fixed-interface (FI) eigenvalues is based upon component test/analysis frequency error, and the dispersion of the HCB stiffness matrix is based on the root mean square (RMS) value of the diagonal of the corresponding cross-orthogonality matrix (DCGM). Details of the process can be found in reference [2]. The LL MPCV model, discussed previously, was based on matching eight test modes derived from low level C4 test data. The median frequency error was 4.65%, and the corresponding DCGM value was 93.87 out of a perfect value of 100. The HL MPCV model was also based on eight test modes, but derived from high level C4 test data. The median frequency error was 5.50%, and the corresponding DCGM value was 96.66. The frequency correlation gets worse going from the LL to the HL model, while the cross-orthogonality gets better.

The absolute percentage frequency error between the ensemble of updated linear MPCV models, described in the previous section, and the surrogate test data for the first nine test modes, relative to the FEM values, is listed in Table 9.7. The test-analysis correlation results between the surrogate test data and the updated linear ensemble models assume that the surrogate test data corresponds to the truth, which it does not. The test data is based upon a nonlinear version of a linear MPCV model; therefore the correlation results are artificially accurate. Note that the absolute mean error is very low at load levels 0.1 and 20 in/s^2, where the joints are essentially totally locked and free, respectively. There is essentially no frequency uncertainty for these two extreme load levels where the MPCV behaves in a more linear fashion. At the intermediate load levels, there is more mixed joint slipping and sticking, leading to more nonlinear behavior. This makes it more difficult to fit linear models, leading to increased frequency errors.

An effort was made to add uncertainty to the test-analysis frequency errors listed in Table 9.7 to reflect the fact that the nonlinear model used to generate the surrogate test data does not match reality. As mentioned, the LL and level 0.1 MPCV models both have the same fixed joint state, while the HL and level 20 MPCV models both have a free joint state. Actual test data from the C4 STA produced a median frequency error of 4.65% in the LL MPCV model and a median frequency error of 5.50% in the HL model. Therefore, 4.65% error was added to all of the frequency errors for level 0.1, and 5.50% error was added to all of the frequency errors in level 20 to account for the difference between the surrogate test data and reality. The median frequency uncertainty was used instead of the mean such that no one mode would have an undue influence. For lack of actual test data at the intermediate load levels, the median frequency error was assumed to vary linearly with load level between the 0.1 and 20 in/s^2 load levels. These intermediate values, listed in Table 9.8, were then added to the frequency errors for each load level listed in Table 9.7. The median frequency error was assigned to all other HCB FI modes that were not matched to a test mode for each load level.

The same approach was used to add uncertainty to the HCB mode shapes for stiffness matrix dispersion. Test-analysis cross-orthogonality between the ensemble of MPCV models and the surrogate test data produced the DCGM values listed in the third column of Table 9.8. As mentioned, these values are artificially high. Based on C4 test-analysis cross-orthogonality, the LL MPCV model had a DCGM value of 93.87, while the HL MPCV model had a DCGM value of 96.66. Assuming that the intermediate load level DCGM values vary linearly between the LL and HL levels, and including the small degradation in DCGM from column 3, produces DCGM values for all eight load levels that account for uncertainty in the surrogate test data, as listed in column 4 of Table 9.8.

The dispersion of the stiffness matrix for each of the HCB MPCV components in the model ensemble was determined by assigning the corresponding component FI frequency uncertainties discussed previously and then assigning a stiffness

Table 9.8 Frequency and mode shape error assigned to account for surrogate test data uncertainty

Load level	Median Freq. Error (%)	Surrogate DCGM	Assumed Test DCGM
0.1	4.65	99.60	93.47
1.0	4.69	99.10	93.09
2.0	4.73	98.42	92.56
3.0	4.77	97.91	92.18
5.0	4.86	98.61	93.22
7.5	4.97	99.20	94.11
10.0	5.07	99.20	94.45
20.0	5.50	99.89	96.55

Table 9.9 Assumed MPCV HCB stiffness matrix dispersions for ascent +50 and ascent +120 s

Load level	A50 Dispersion (%)	A120 Dispersion (%)
0.1	3.25	2.25
1.0	3.00	2.00
2.0	2.90	1.75
3.0	2.75	1.75
5.0	1.25	1.00
7.5	0.00	0.00
10.0	0.00	0.00
20.0	0.00	0.00

dispersion value. Using that uncertainty model, a MC analysis with 3000 iterations was used to generate an ensemble of nominal-random cross-orthogonality matrices, which produced an ensemble of random DCGM values corresponding to the selected dispersion value. The most probable DCGM value corresponding to the first 64 free-free elastic non-slosh modes with frequencies less than 20 Hz. was computed over the ensemble and compared to the assumed test values listed in column 4 of Table 9.8. The stiffness dispersion value for the component was adjusted until the most probable and test DCGM values agreed. Details of the process can be found in reference [2].

Ascent at T0 + 50 and T0 + 120 s were considered in the subsequent buffet and GNC SOP analyses, respectively. The stiffness dispersion values selected for each of the MPCV HCB models in the ensemble are listed in Table 9.9. Note that the dispersion values decrease as the load level increases, to the point where no stiffness dispersion is required to obtain the desired component mode shape uncertainty. This is consistent with the previous uncertainty models derived for the LL and HL MPCV components. As mentioned previously, there are four other HCB components within the SLS system models. The corresponding uncertainty models were derived using component modal test results. Details related to these components and their uncertainty models can be found in references [2, 3].

9.4.3 SOP UQ Analysis for Additional Model Ensemble Members

The SOP analysis for the guidance, navigation, and control stability conditions was repeated for the eight additional systems, each containing one of the MPCV ensemble models. The uncertainty in the fundamental bending mode frequencies must be greater than −10%, and the corresponding frequency response gain uncertainty must be less than 4 dB for control system stability. Figure 9.17 corresponds to Fig. 9.3 for pitch frequency uncertainty, but with the CCDFs from the eight additional models. Only two of the CCDFs, load level 0.1 and load level 1 in/s^2, lie slightly outside the region bounded by the CCDFs corresponding to the LL and HL MPCV models. This implies that if a linear MPCV model is a valid representation of the nonlinear MPCV at a specific load level, then the LL and HL MPCV models essentially bracket the effect of the MPCV nonlinearity on the fundamental pitch frequency. Figure 9.18 presents an expanded view of Fig. 9.17 for the critical region of negative frequency uncertainty. It can be seen that within this region, all of the CCDFs are to the right and above the CCDF corresponding to the HL MPCV model. This implies that for a specific negative frequency uncertainty, like the critical value of −10%, the HL model yields a lower probability that the actual pitch frequency uncertainty is greater than that value. Therefore, in terms of control system stability, using the HL MPCV model, and its corresponding uncertainty model, produces a statistically more conservative result with respect to pitch frequency uncertainty.

Figure 9.19 is analogous to Fig. 9.5 for yaw frequency uncertainty, but with the additional eight model CCDFs. In this case, three of the CCDFs, corresponding to load levels 0.1, 1, and 2 in/s^2, lie outside the region bounded by the LL and HL MPCV

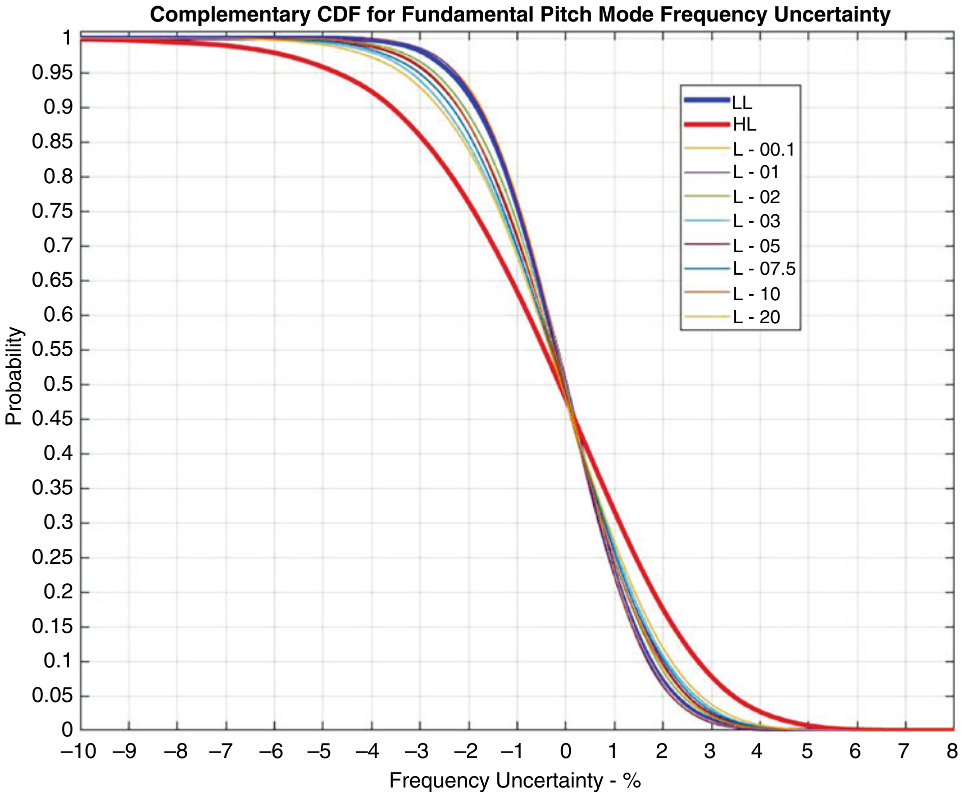

Fig. 9.17 Complementary CDFs for pitch frequency uncertainty

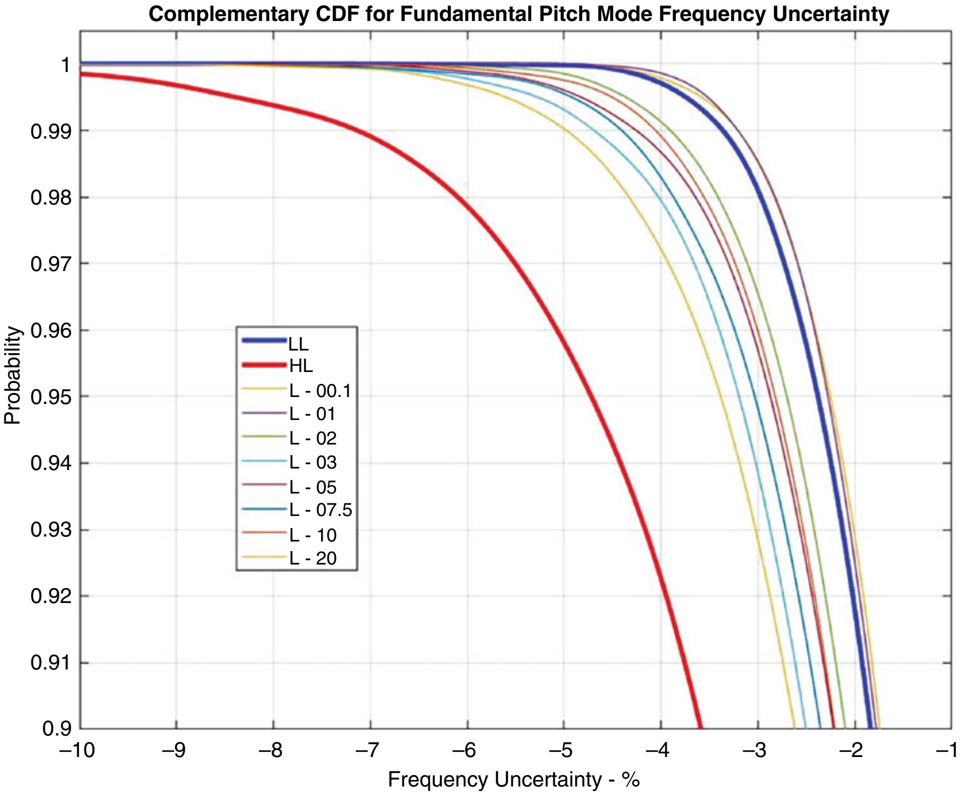

Fig. 9.18 Expanded view of complementary CDFs for pitch frequency uncertainty

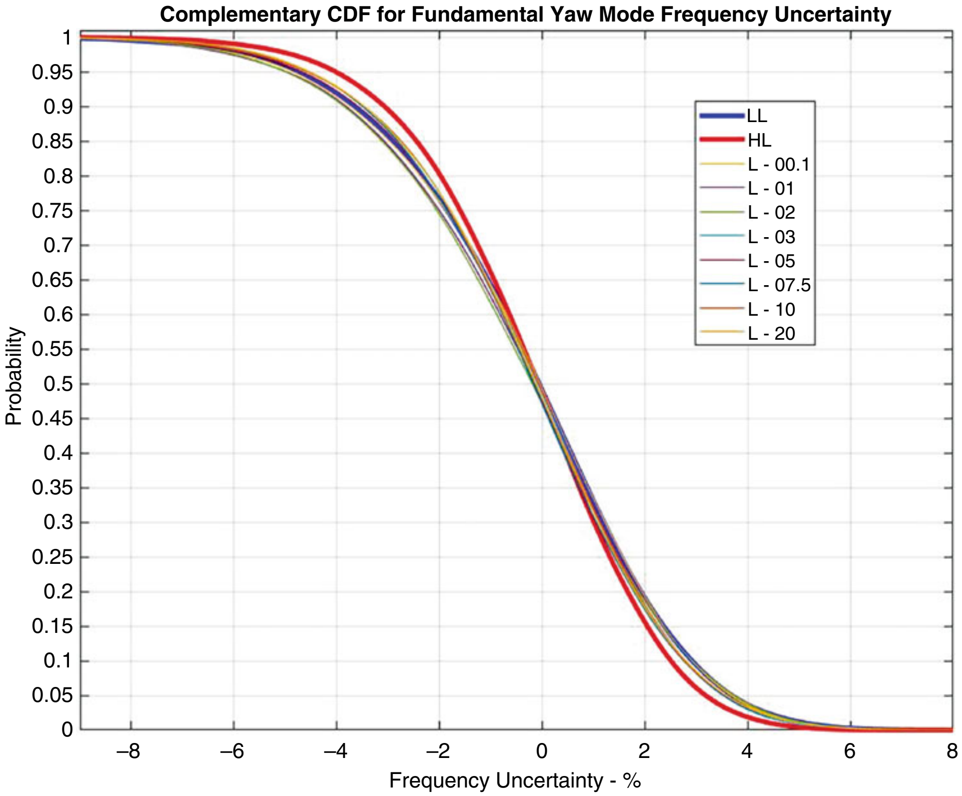

Fig. 9.19 Complementary CDFs for yaw frequency uncertainty

CCDFs. Figure 9.20 presents an expanded view of Fig. 9.19 for the critical region of negative frequency uncertainty. In this case, within the region of negative frequency uncertainty, all the CCDFs are to the left and below the CCDF corresponding to the HL MPCV model. This implies that for a specific negative frequency uncertainty, the HL model yields a higher probability that the actual yaw frequency uncertainty is greater than that value. Therefore, in terms of control system stability, using the HL MPCV model produces a statistically less conservative result with respect to yaw frequency uncertainty.

Figure 9.6 shows the LL and HL MPCV model CDFs for pitch rate gain uncertainty at the itRGA. Figure 9.21 presents the expanded view of Fig. 9.6 for the critical region of positive gain uncertainty, including the CDFs for the ensemble of MPCV models. As in the case of pitch frequency uncertainty, all of the ensemble CDFs lie between the LL MPCV and HL MPCV CDFs, with the exception of the CDFs corresponding to the 0.1 and 1 in/s^2 load levels, which are outside, but close to the LL CDF. The figure shows that all of the CDFs are to the left and above the CDF corresponding to the HL MPCV. This indicates that for a specific value of positive rate gain uncertainty, such as the critical value of 4 dB for control system stability, the probability of that uncertainty value being exceeded is greater using the HL MPCV model than when using the other MPCV representations. This implies that using the HL MPCV and its corresponding uncertainty model is statistically more conservative than the other models with respect to pitch rate gain uncertainty at the itRGA. Figure 9.22 illustrates the expanded view of Fig. 9.7 for the region of positive yaw rate gain uncertainty at the itRGA but including the CDFs for the ensemble of eight MPCV models. For the most part, the ensemble CDFs lie between the LL and HL MPCV CDFs. At probabilities below 2% and above 90%, the ensemble CDFs venture outside the LL/HL CDF interval, but the departure is never very great. Also, for the most part, the HL MPCV CDF lies to the right and below the other MPCV CDFs within the positive rate gain uncertainty region. This indicates that using the HL MPCV model is also statistically conservative with respect to the yaw rate gain uncertainty stability criterion at the itRGA.

The application of the SOP approach to the buffet CS section loads for the LL and HL versions of the SLS at ascent T0 + 50 s configuration was described in the previous section. As discussed, the original analysis [3] found that there were substantial differences in nominal CS peak moments about Y and in peak shear along Z predicted using the LL versus the HL MPCV models. The maximum peak moment about Y occurs at section $x = 2754.99$ inches using the LL MPCV model. The SOP analysis was repeated for the eight additional systems, each containing one of the MPCV ensemble models. Figure 9.23 illustrates the LL and HL CDFs, as well as the CDFs from the eight additional ensemble models, for the peak moment about Y at $x = 2754.99$ inches for 1000 random systems. Apart from very low probabilities, all but two of the ensemble

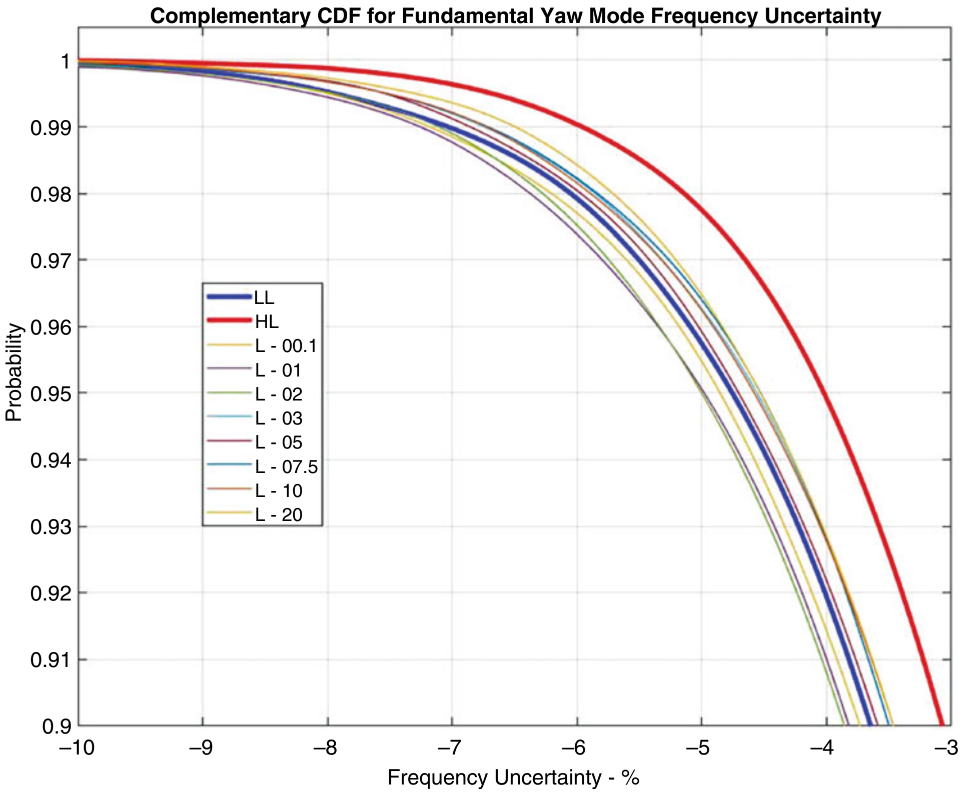

Fig. 9.20 Expanded view of complementary CDFs for yaw frequency uncertainty

model CDFs, levels 0.1 and 1 in/s^2, are bounded by the LL and HL MPCV CDFs. With the same exception, the HL MPCV CDF lies to the left and above all other CDFs. This indicates that for a specific value of peak CS section moment about Y, the probability that the value is exceeded is smaller for the HL MPCV model than all other models. The HL MPCV model is therefore less conservative statistically with respect to CS peak section moment about Y at the specific section $x = 2754.99$ inches.

The maximum peak CS shear along Z occurs at section $x = 2862.71$ inches using the HL MPCV model. Figure 9.24 presents the LL and HL CDFs, as well as the CDFs from the eight additional ensemble models, for the peak shear along Z at that section. Up to a probability of P99.6, only two of the ensemble model CDFs, levels 0.1 and 1 in/s^2, are not bounded by the CDFs of the LL and HL MPCV models. The corresponding excursions are small, and for the most part, only the level 0.1 CDF is outside the region between the LL and HL CDFs. In addition, the HL MPCV model CDF lies to the right and below all other MPCV model CDFs. This indicates that for a specific value of peak CS section shear along Z, the probability that the value is exceeded is larger for the HL MPCV model than all other models. The HL MPCV model is therefore conservative statistically with respect to CS peak section shear along Z at the specific section $x = 2862.71$ inches.

While only a small number of SLS response items were considered in this assessment, the HL MPCV and corresponding uncertainty models produced statistically conservative results most, but not all of the time. Statistical conservatism implies here that, for example, if there is a particular response item that is not to be exceeded, using the HL MPCV and uncertainty models produces a greater probability than other possible models that it will be exceeded.

9.5 Conclusion

Epistemic and aleatory uncertainty cannot be handled in the same manner within a UQ analysis. However, epistemic and aleatory variables can be combined within a single UQ analysis using a SOP approach. The nonlinearity within the MPCV is a model-form or epistemic uncertainty. In this assessment, it is assumed that the MPCV nonlinearity can be represented by an ensemble of linear MPCV models, one for each forcing level of interest. Sampling the ensemble of MPCV models and then performing an HPV UQ analysis produces an ensemble of CDFs for the associated QOIs. A p-box analysis of the

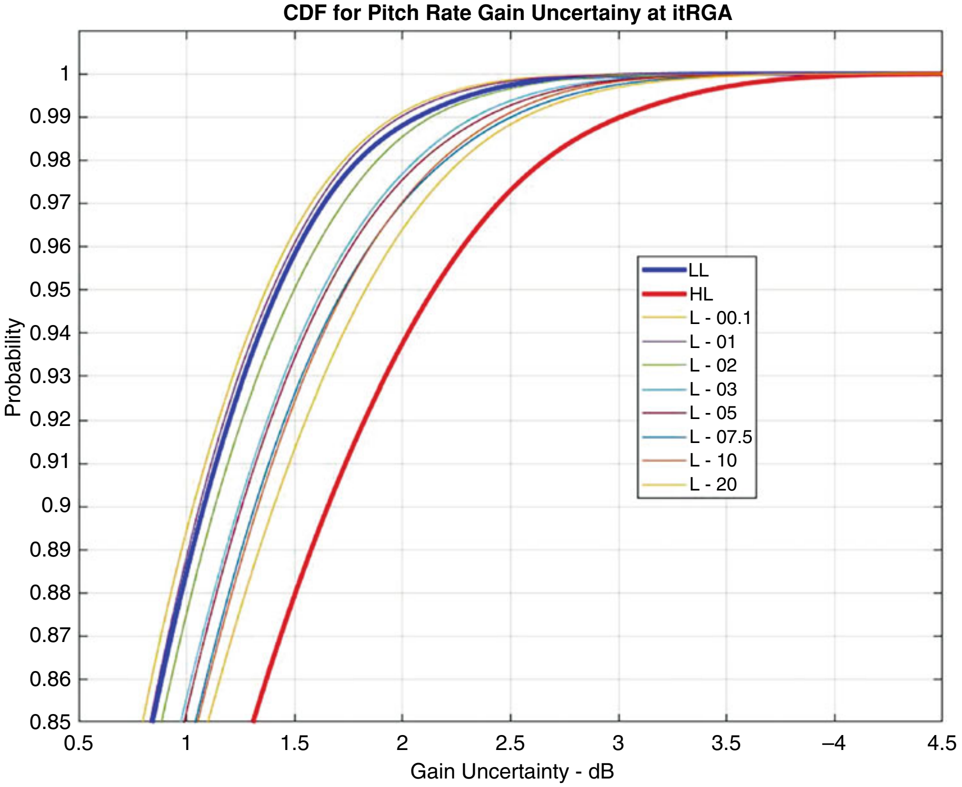

Fig. 9.21 Expanded view of CDFs for pitch rate gain uncertainty

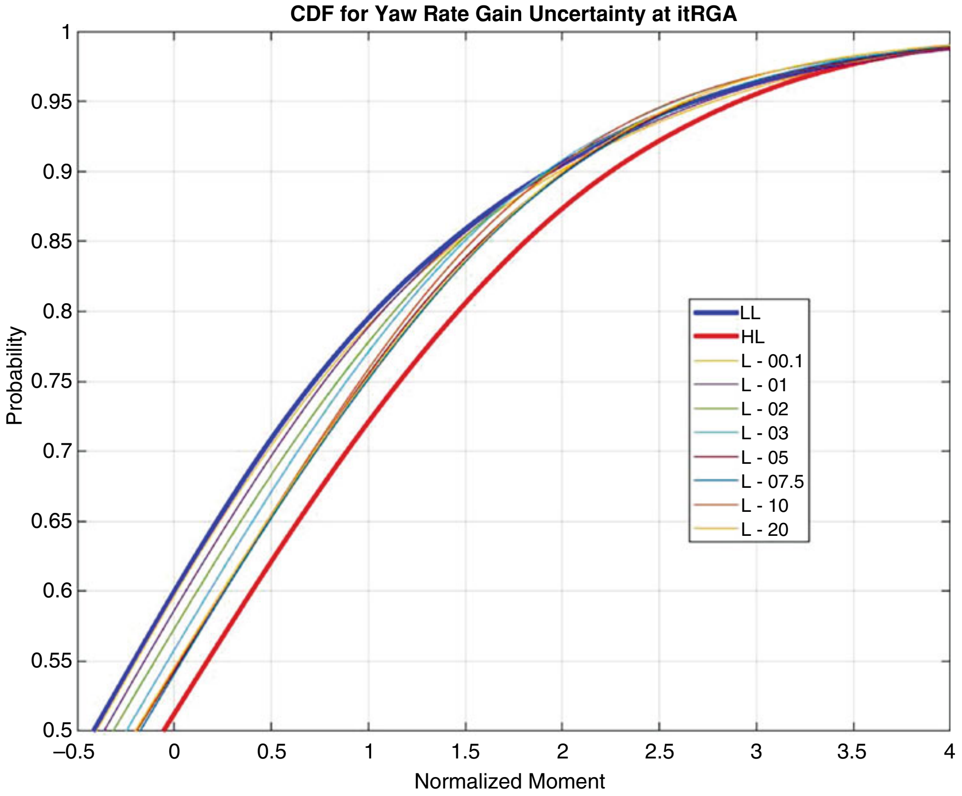

Fig. 9.22 Expanded view of CDFs for yaw rate gain uncertainty

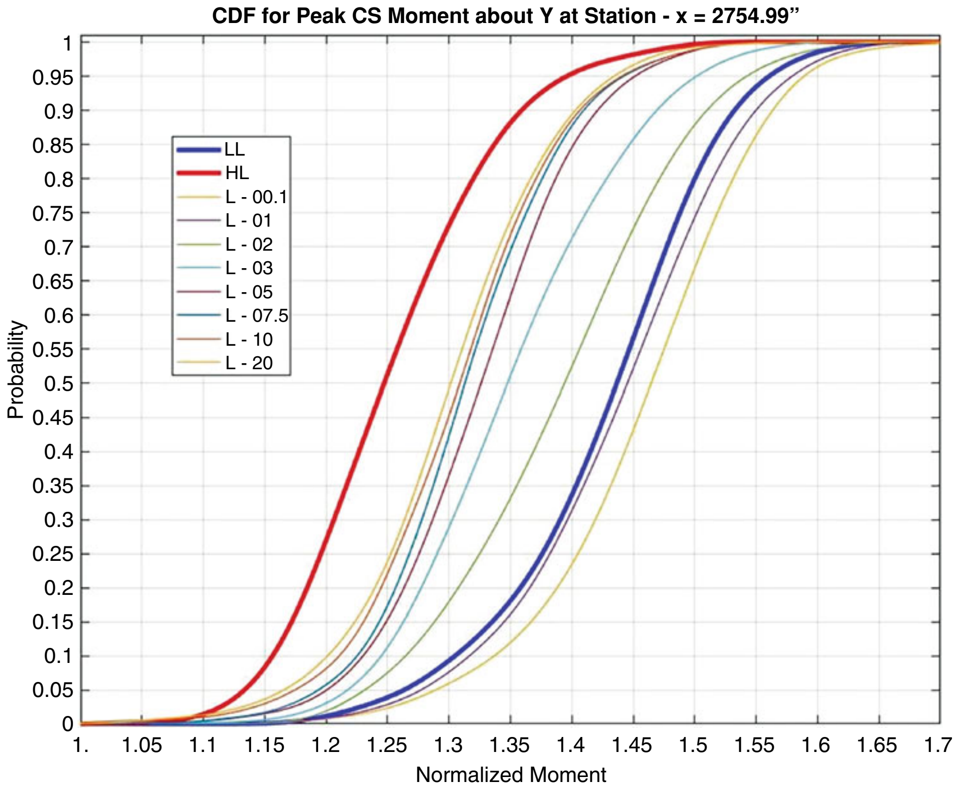

Fig. 9.23 CDFs for peak CS moment about Y at $x = 2754.99$ inches

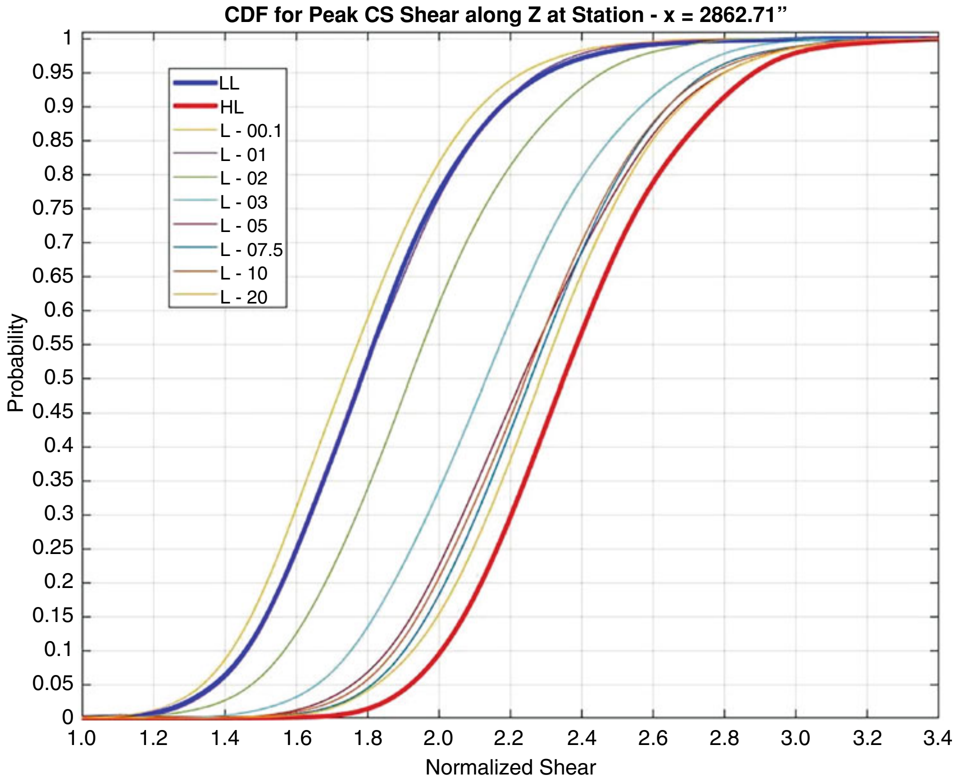

Fig. 9.24 CDFs for peak CS shear along Z at $x = 2862.71$ inches

upper and lower bound CDFs produces plausible ranges of probability for specific QOI values and plausible ranges of QOIs for specific probabilities. The larger the ranges, the greater the impact of the MPCV nonlinearity upon the QOIs.

In the case of the SLS, there were initially only two MPCV models within the SOP outer loop ensemble corresponding to low and high C4 test forcing levels. Using the CDFs from these two models, a p-box analysis was performed for selected QOIs to assess the influence of MPCV nonlinearity. However, there was no guarantee that the LL and HL MPCV models represent the true bounds of the model-form uncertainty due to the nonlinearity. Ideally, additional C4 modal test data would have been measured at intermediate loading levels. To determine how well the LL and HL MPCV models bound the response of the actual nonlinear MPCV, the C4 test data was augmented with surrogate test data generated using a nonlinear model of the MPCV. Eight additional linear MPCV models were derived based on simulated response to enforced base sine inputs. SOP UQ analysis was performed for each of the additional eight models in the ensemble. The UQ analysis also included uncertainty models of all the other SLS components that had previously been derived using modal test data. The corresponding horsetail plots showed that for the specific QOIs selected, at least six of the eight additional intermediate model CDFs were bounded by the LL and HL MPCV model CDFs. When an intermediate load level CDF was outside the interval, it was only slightly outside the boundary formed by the LL MPCV CDF. Therefore, if it can be assumed that a linear MPCV model can adequately represent the response of the nonlinear MPCV at a specific load level, then the ensemble of linear models in the outside SOP loop spans the response of the nonlinear MPCV. The p-box formed by the ensemble CDFs bracket the response of the nonlinear system. In the cases examined, the LL and HL MPCV CDFs for the selected QOIs are close to bracketing the nonlinear system response and representing the associated model-form uncertainty. The HL model CDFs always bounded the other models, while up to three intermediate level models had CDFs outside the region bounded by the LL model. It was also found that the HL MPCV model does not always give statistically conservative results.

This assessment shows that the SOP approach combined with the HPV UQ method can provide an effective means of determining the impact of component nonlinearities upon the uncertainty in system level results.

References

1. Craig, R.R., Bampton, M.C.C.: Coupling of substructures for dynamic analysis. AIAA J. **6**, 1313–1319 (1968)
2. Kammer, D., Blelloch, P., Sills, J.: Test-based uncertainty quantification and propagation using Hurty/Craig-Bampton substructure representations. In: IMAC, Orlando, FL (2019)
3. Kammer, D., Blelloch, P., Sills, J.: Variational coupled loads analysis using the hybrid parametric variation method. In: IMAC, Houston, TX (2020)
4. Kammer, D., Blelloch, P., Sills, J.: SLS integrated modal test uncertainty quantification using the hybrid parametric variation method. In: IMAC (2020)
5. Ferson, S., Ginzberg, L.: Different methods are needed to propagate ignorance and variability. Reliab. Eng. Syst. Saf. **54**, 133–144 (1996)
6. Peterson, L.D., Mobrem, M.: A Comparison of Uncertainty Quantification Methods on Benchmark Problems for Space Deployable Structures, 2018 AIAA Spacecraft Structures Conference, Kissimmee, FL, January (2018)
7. Eldred, M., Swiler, L.: Efficient Algorithms for Mixed Aleatory-Epistemic Uncertainty Quantification with Application to Radiation-Hardened Electronics-Part I: Algorithms and Benchmark Results, Sandia Report: SAND2009_5805, September (2009)
8. Bailey, E., Peterson, L.: Ignorance vs. Variability: Considerations for UQ Analysis, Joint GN&C and L&D Uncertainty Quantification Workshop, Marshall Space Flight Center, January 17, (2018)
9. Moderes, M., Bergerson, J.: Dynamic analysis of uncertain structures using imprecise probability. Int. J. Reliab. Saf. **9**(2/3), 203–219 (2015)
10. Chapman, J.M.: Incorporating a Full Damping Matrix in the Transient Analyses of Nonlinear Structures, Damping '93 Conference, San Francisco, (1993)